PROCEEDINGS, 50th Workshop on Geothermal Reservoir Engineering
Stanford University, Stanford, California, February 10-12, 2025
SGP-TR-229

Drilling Target Mapping at Newberry with Passive Seismic Permeable Fracture Imaging (PFI)

J. Eppink, T. Fleure, P. Malin, A. Mathews, W. McLain, C. Sicking, and A. Stroujkova

Enegis, LLC, 10300 Eaton Place, Fairfax, VA 22030

JEpping@enegis.com

Keywords: Passive seismic method, emissions from fluid-filled fractures, data collection, signal processing, PFI results

ABSTRACT

We present a beginning-to-end case history of PFI mapping of potential drilling targets at Newberry Volcano, Oregon, in 2023. The PFI method uses hundreds of time-synced seismic recorders to observe episodes of small seismic movements in connected permeability structures – the fluid filled joints, fractures, fracture zones, faults, and fault zone that are geothermal drilling targets.

PFI signals are initiated by local changes in crustal stress. Such perturbations can be caused by near and distant earthquakes, industrial activities, rapid moving air masses, tidal loading, fault creep, and the like. These second-to-hours long disturbances superimpose stress changes on the longer-term tectonic stresses. The resulting PFI signals can continue for tens of seconds to minutes as the permeability structures readjust to the new stress field.

Our 2023 Newberry survey was designed to locate these signals for potential drilling targets. It was supported by ARPA-E grant AR000166 with supplementary funds from Quaise Energy. Early in 2023 we modeled the location and resolution tradeoffs for several distributions of seismic velocity, PFI signal depths, recorder spacings and network size. Based on them we deployed 982 can-sized seismic recorders, nominally 175 m apart, over a 27 km^2 area west of Lake Paulina. This network captured PFI-signals above a ~2.1 km deep, ~2.75 km^2 patch centered on the 3 km deep 55-29 well.

The recorders were deployed by a crew of 12 over 6 days in Oct 2023 with a station accuracy of 2 m. The completed network ran for 5 days. On day 4, a 3-hour long, low pressure hydraulic stimulation was done in 55-29. Retrieval took 5 days, just days before a 4" snow would have hidden their exact locations.

The initial phase of data download, quiet time selection, trace editing, and noise suppression was completed in Nov. PFI signal locations were then found by first searching for high semblance episodes in the recordings. Using the velocity model, these episodes were then traced back to their originating ~10x10x10 m voxel in a 165x165x185 volume of 5,036,625 voxels. In late Jan, maps and cross sections through this PFI signal volume were made using color bar, isosurfaces, and maximum semblance track methods and used for geological interpretation.

The PFI maps and sections were compared to geological ones, 55-29 well logs, and a magnetotelluric resistivity profile. The PFI maps have trends matching known NNW striking, east-dipping normal faults. Near-well PFI horizons correlate with the well logs and lithology. A low resistivity body in the MT profile correlates with an absence of PFI signals, interpreted as a clay cap with limited permeability. Three other high semblance targets were also observed beyond 55-29.

From funding to establishing potential drilling targets, the Newberry PFI study took ~1-year, the bulk of which was for permitting. Points along the project's critical path included permitting, establishing a velocity model, testing tradeoffs of PFI resolution, depth, recorder numbers and spacing, and processing. With a follow-on ARPA-E award we are planning a second, deeper, Newberry PFI study in 2025.

1. INTRODUCTION

The heterogeneous permeability field of the Earth's brittle crust has long been a challenge for the extraction of fluid resources. Permeable Fracture Imaging (PFI) helps overcome this challenge by directly mapping permeability related structures – fluid-filled fractures, joints, and faults [1]. PFI uses many hundreds of seismometers (typically more than 1,000) to passively listen for *minute seismic tremors* from these features [2]. The tremors are episodically created by the earth's flux of stresses due to earthquakes, fluid flows, and gravitational forces. They can also be initiated and driven by industrial activities such as hydraulic fracture stimulation and well field operations. The tremors can continue for many seconds, making it possible to use reflection seismic methods – albeit with 1-way rather than 2-way travel times – to map their subsurface locations. When compared with other geological and geophysical information, the map can be interpreted in terms of physical properties correlated with structure, lithology, resistivity, and hydrology.

In this paper we illustrate the PFI method with a case history of the Newberry geothermal prospect, beginning with planning and ending with the interpreted results. The presentation is heavy on visual material as this best convey our results – the captions are important!

2. PROJECT PLANNING: GEOSCIENCE BACKGROUND AND PFI DATA COLLECTION DESIGN

Early on in our interactions with our industrial collaborators, it became clear that our PFI survey would best support geothermal development at Newberry if it was centered around Newberry Well 55-29 [3]. This choice also offered the opportunity to evaluate the PFI map in terms of other near-well observations [4, 5]. Once settled, the project focus was then on 4 preparatory studies: 1. Assembling

and digesting all the available topographic, hydrological, geological, and geophysical data and models for the well site.; 2. Using these data to develop the best seismic velocity model for designing the survey and processing the PFI data; 3. Using the existing seismic monitoring stations to assess the background noise; and 4. Design the PFI seismic network and establish the stations for permitting.

2.1. Structural Geology, Lithology, and Electrical Resistivity.

Newberry Volcano is a large shield volcano. Located in central Oregon, Newberry is situated near the conjunction of three distinct geologic zones. This includes the Cascade Volcanic Arc to the west, the Basin and Range province to the south and southeast, and the Columbia Plateau in the northeast and east. It is at the interface of two structural settings: the north-trending, east-west extension of the Cascade Arc, and the northwest-trending normal faulting within the Brothers Fault system of the Basin and Range province. This structural setting has heavily influenced the geology of the region as well as the formation of the Newberry volcano.

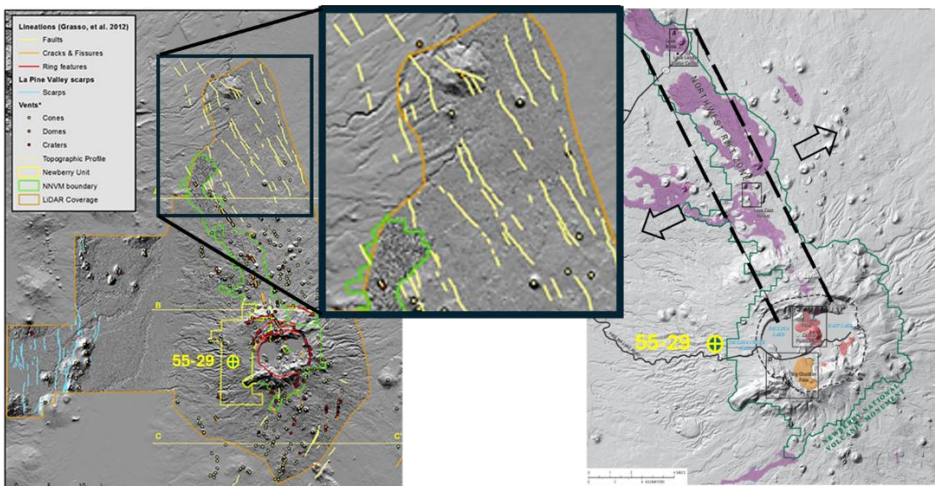

Figure 1. Regional Newberry normal fault zones trends and the Northwestern Rift Zone. (Figures from [6, 7, 8])

As seen in Figure 1. This volcano is built on top of a north-northeast-west-southwest extending crust, with north-northwest trending normal faults and volcanic rift. The major regional scale faulting is east dipping, as shown in the schematics E-W geological cross section in Figure 2c. Cross sections 2a and c also show the interpreted configuration of the major subsurface formations that were drilled through by Well 55-29. As will be seen in the project results, the faults and trends form major features in the PFI map.

The electrical resistivity of the volcano's west flank and area around Well 55-29 was previously studied using magnetotelluric methods (MT). At Newberry, there is a shallow, electrically conductive layer that is underlain by an electrically resistive mass. A three-dimensional diagram of the resistivity results is given in Figure 2b [3]. The perspective is from the southwest looking northeast. The electrically conductive zone, interpreted as a clay alteration, is in red/brown colors, red denoting the highest conductivity. A well-log density and lithology observed in the 55-29 well are shown in Figure 3. Our PFI interpretation uses the fault, resistivity, density and lithology data.

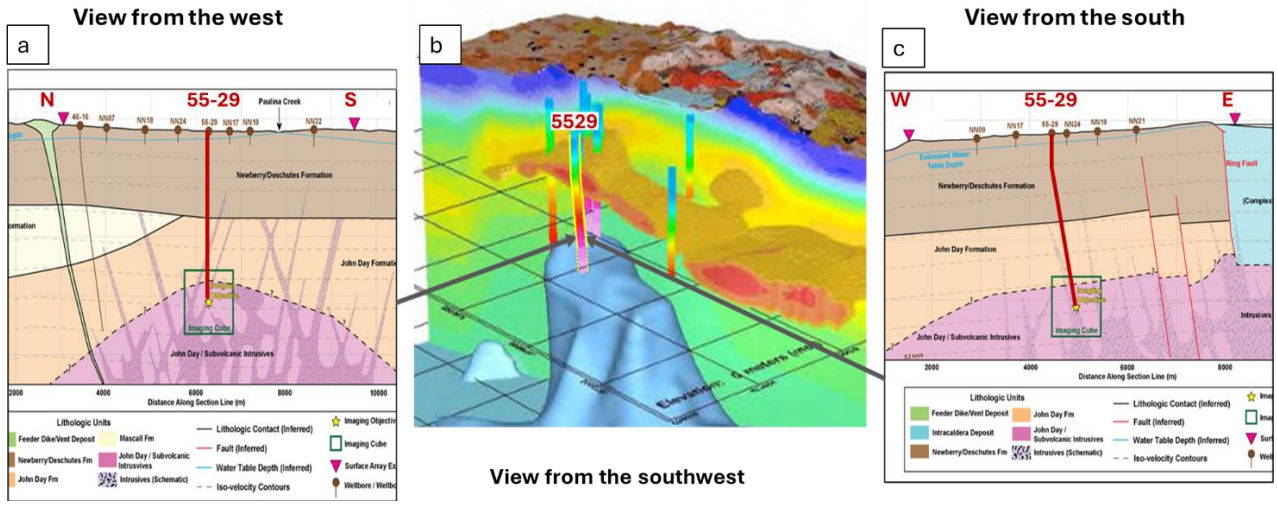

Figure 2. Cross sections through Well 55-29 (a&c) and a block diagram of electrical resistivity (b). Well 55-29 is interpreted as having drilled into the top of an intrusion's subsurface cupula. The caldera wall appears on the far-right side of 2c. [3]

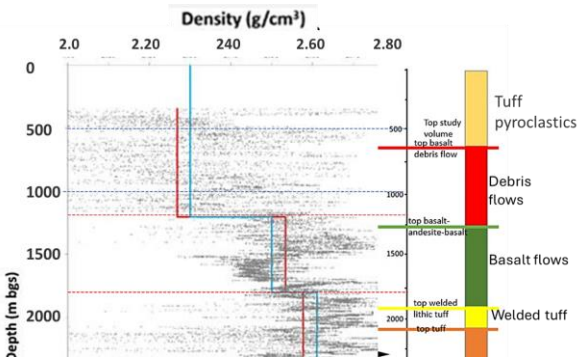

Figure 3. The density log and lithology observed in the 55-29 well. [5]

2.2 Seismic Velocity Model

To design a PFI passive seismic data collection network of seismographs, a first order seismic velocity structure was needed. In this task we were added by 3 major studies using combinations of teleseismic, local earthquake, and controlled explosion travel time data. We also were able to use old quarry blast data to add an additional constraint. These models and the geometry of the quarry and its seismic observation stations are shown in Figure 4. Well 55-29 is in the center of the cluster of stations shown in Figure 4a.

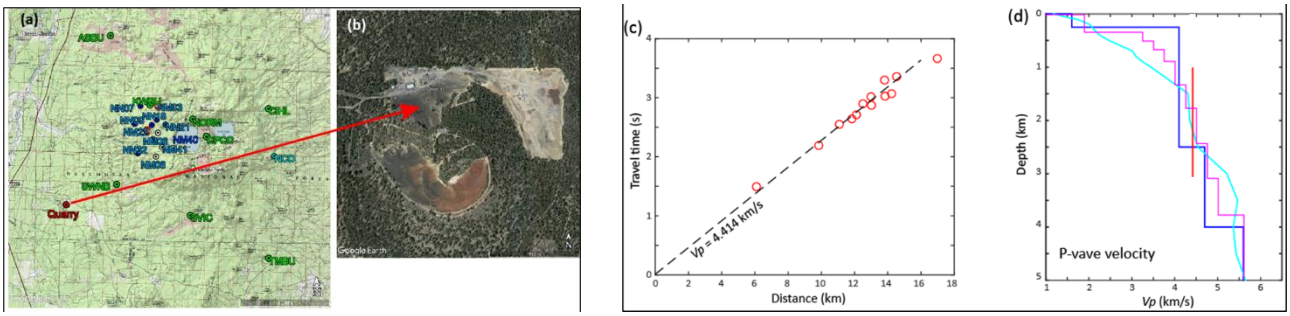

Figure 4. (a) A map of the seismic stations that recording the quarry blast on 2014.09.16. Well 55-29 is in the center of this net. Note that there is a railroad paralleling the highway (black line) on the west side of this map. Our noise study revealed that daily train traffic on this railway significantly interfered with PFI data collection. (b) A Google Earth image showing the quarry to which we attribute the blast to. (c) P-wave travel times vs distance for the blast. (d) Seismic velocity structures from 3 prior studies (blue, magenta, cyan) plus the estimated velocity from the blast (red). The limited offsets of the blast data restrict its velocity-depth coverage to roughly 1 to 3 km, validating the magenta/cyan velocity models in the 1.5-2.5 km interval. [10-19]

2.3 Seismic Background Noise.

In addition to having a 1st order seismic velocity model, design of the PFI data collection network also depends on characterizing the seismic background noise. Seismic noise can significantly degrade the quality of seismic measurements and affect the performance of ambient noise imaging. Seismic noise can be divided into cultural and natural. The sources of cultural noise include moving vehicles and operating machinery (pumps, generators etc.). Natural noise includes weather-related noise (rain, wind, waves) as well as earthquakes.

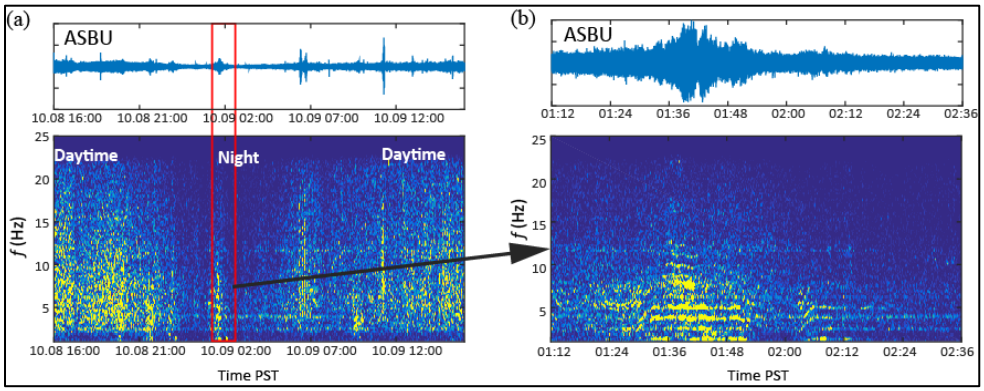

Figure 5. (a) A spectrogram of a 24-hour period for a broadband surface station near Well 55-29. (b) A zoomed in view of the nighttime spectrogram window highlighted with red in (a) that shows harmonic signals that we have identified as train noise.

Many of the stations shown in Figure 4a have remained active and include a few borehole seismographs. We used them to study both the cultural and natural seismic noise background at Newberry. Some examples of the cultural noise are presented in Figures 5 and 6 (Stroujkova personal communication 2024). Figure 5a shows a spectrogram (a frequency versus time display) of a 24-hour time interval of data from a broadband station located near well 55-29. There are two interesting features in this spectrogram: the decreased noise level during the nighttime (5a) and a long series of harmonic ground vibrations (5b).

The nighttime quiet is of course common near places were people live and visit, and Newberry is no exception. After careful study, including trying to get train schedules from the rail operator (absolutely denied) and deploying 5 seismometers along the train tracks, we established that these signals are produced by passing trains on the tracks mentioned in Figure 4. Figure 6a reveals that the train signals are indeed harmonic, with frequencies of 1.2, 2.4, 3.6, and 4.8 Hz.

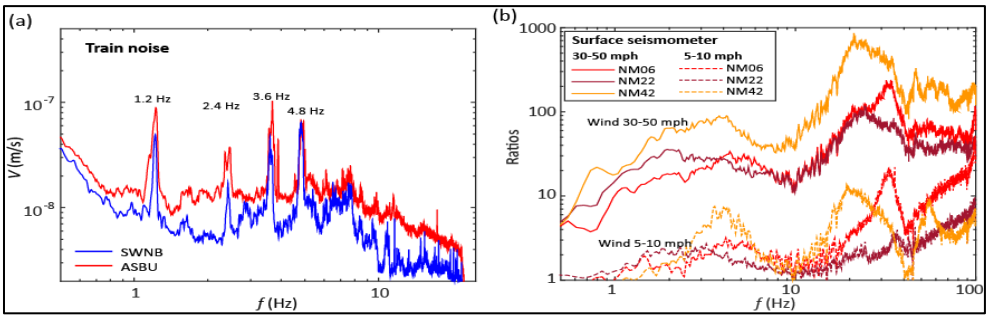

Figure 6. (a) The spectrum of harmonic signals from rail traffic several miles to the west of our Newberry PFI survey site. (b) a spectral analysis of wind noise. The curves show ratios of seismic noise between calm and high wind speeds. Note the log scales in both frequency, ground velocity, and wind speed noise ratios.

Wind is another source of seismic noise affecting the data quality. To study the effect of wind on seismic data we used (1) the historical data from the closest weather station with a digital record, the Roberts Field Station in Redmond, OR and (2) the Figure 4a seismic network noise data recorded between September and November 2014. Since the Roberts Station is about 100 km from the 55-29 borehole, the wind speeds at the Well site may exhibit time lags and amplitude differences. However, during this period two regional windstorms with wind gusts exceeding 50 mph were reported, first on 25 October and second on 11 December. We used these data to assess the frequency distribution of seismic noise versus wind speed (Figure 5b).

In Figure 5b, we plot the ratios of noise between windy conditions and calm for 3 widely separated Newberry seismic stations. For the winds on the order of 5 – 10 mph the noise amplitude in the frequency band 15 – 40 Hz increases by a factor of 5 – 10. For the intense winds (30 – 50 mph) the noise amplitudes exceed the reference noise by a factor of 100 – 1000. These observations suggest, obviously, that the time intervals with high winds should be eliminated when processing the PFI data. However, they suggest that at moderate wind speeds, ambient PFI signals, which are commonly at frequencies below about 30 Hz, are not nearly as badly effects as those at higher frequencies. Hence the station spacing did not need to be reduced to allow correction for the high frequency wind noise.

2.4 The PFI Seismic Receiver Network Design, Field Station Locations, and Deployment Strategy.

The two independent types of data discussed in **2.3** and **2.4** – velocity and background noise - are used to determine the total area of the network and the station spacing. These two factors, area and spacing, control the tradeoff between the depth of PFI resolution and the number of seismic stations needed for the project. In our case the number of stations was fixed by our ARPA-E budget, so the network station spacing determined the tradeoff between the maximum depth of the PFI map and its resolution.

Determining PFI spatial resolution uses methods adapted from 3-D reflection seismology: it is based on the tradeoff between source frequency, minimum source-receiver offset, receiver number and spacing, and target depth. Given our expected source frequency (<30 Hz) and minimum offset (> target depth), along with a budget for about 1,000 receivers, the choice of resolution balanced receiver spacing with target depth. With a resolution set at a few tens of meters (40 m), the corresponding receiver spacing (175 m) determined the maximum target depth (~2,100 m). The resulting receiver network and different areas of relative imaging resolution is shown in Figure 7, along with a field logistics plan for deployment.

The network covered 27 km and had a total of 982 stations (Figure 7a). At its center, by adding (stacking) signals from a large subset of these stations, those contained in a *stacking aperture*, the network produces a maximum signal-to-noise improvement of ~25 - a 625-fold stack (Figure 7b). The size of the aperture is set by the maximum distance over which two stations can detect signals from a common subsurface point. The stacking improvement falls off toward the network edges as the number of receivers in the aperture and thus fold decreases, reducing the depth of highest resolution (a minimum 225-fold stack at the edge, Figure 7c).

The positioning of the stations can be varied by as much as 5-10% of the station spacing to accommodate for permitting and efficient deployment along roads without degrading the final processed PFI map. This adjustment can be seen in Figures 7a and 7d, with 7d showing how the net was broken up into blocks for assignment to 6 different receiver deployment teams.

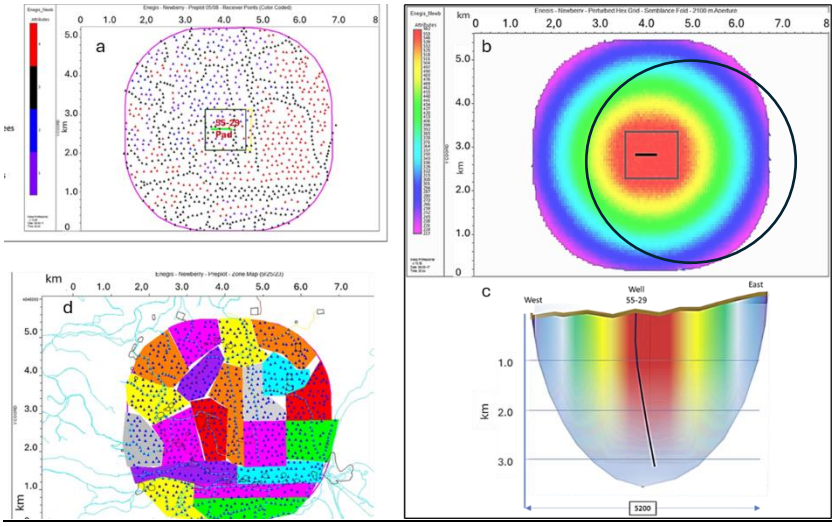

Figure 7. (a) The PFI network footprint and station locations adjusted to road access for time-efficient deployment. (b) A color code map of stacking fold. The black circle –called the aperture - illustrates how the number of stations within it, all of which are used to make the stack, falls off as it approaches the network edges. The stacking fold ranges from red > 575 to purple > 225. (c) the depth/resolution ellipsoid associated with the signal processing aperture as the number of receivers inside of it falls off toward the networks edges. (d) a logistics division of the network into ~50 station-containing blocks for efficient deployment.

3. THE NEWBERRY FIELD CAMPAIGN.

The passive seismic PFI method calls for recording continuous data as many receivers for as long as economically possible. At Newberry this amounted to 982 receivers all running together for 5 days. This network was built up over 5 initial days, run for 5 more at full strength, and then retrieved in 4 more days – the latter as it turned out a few days before the field site got covered with snow. The components and steps of the deployment and retrieval are shown in Figure 8.

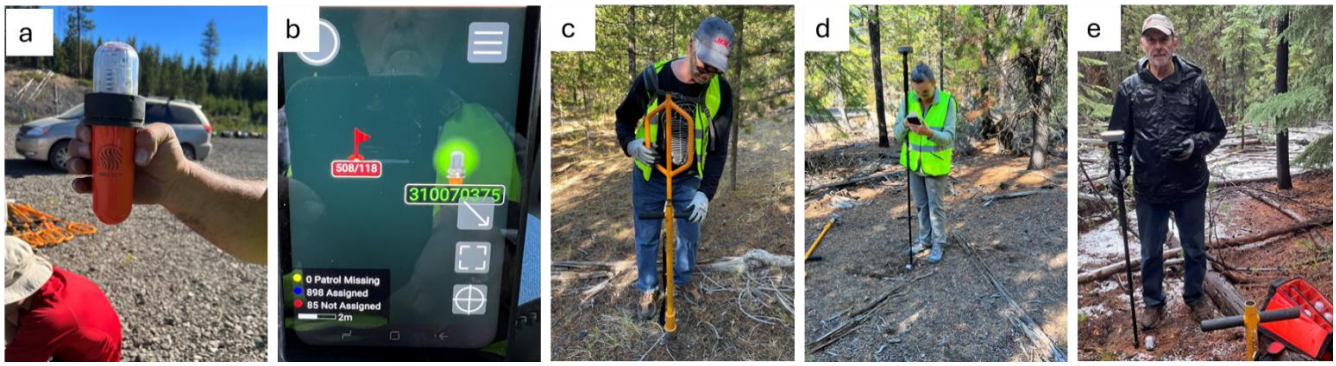

Figure 8. (a) A NuSeis seismic receiver: GPS, computer, battery, vertical geophone. (b) Handheld station locator and directions. (c) Slide hammer for punching secure receiver hole. (d) registering installed receiver at base of GPS guide pole. (e) Retreval: GPS guide pole, map directions handheld cell phone, 10 station carrying sack.

4. PFI SIGNAL PROCESSING

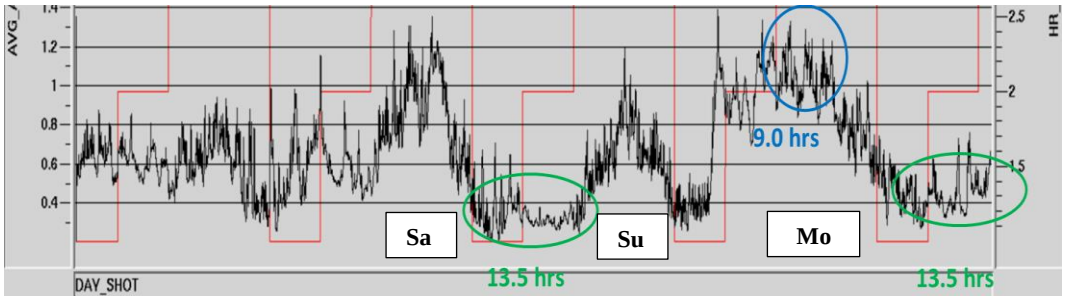

Figure 9. Total signal energy for 4.5 days (108 hrs) of continuous data recording at 500 Hz. 27 hrs were selected for final processing. The peak cultural noise periods was on Sa and Su, 14 and 15 Oct, due to ATV and other vehicles in the area. On Mo 16 Oct there was a windstorm. The quietest was Sa night and careful noise editing on Mo night gave similarly useful data.

4.1 Noisy Data Sections Removal and Filtering.

We analyzed seismic amplitudes from all array nodes during the experiment to determine the noisy locations and time intervals. Figure 9 shows the net root mean square amplitudes averaged over each minute during the full array spread. Notice the diurnal pattern with higher amplitudes during the day and lower amplitudes at night. Strong cultural noise is observed on Saturday afternoon with the highest amplitudes following the road and various tourist attractions in the southern part of the array. The lowest noise data was recorded on Sa and Su nights, the latter being interrupted by an early morning windstorm that eliminated all the data until Mo night. In the end, careful noise editing and filtering on Mo night brought these data to useable signals. In total, of the 108 hrs of recording 27 hrs gave the best promise for further processing.

The next step in the noise reduction is Cepstral Filtering, which is used to remove stationary noise persistent for long periods of time. This type of noise is common in populated areas and appears as noise background added to the slowly changing, harmonic character of fracture seismic signals (C. Sicking, personal communication, 2019). Figure 10 shows spectrogram result of Cepstral Filter application to a Newberry seismic trace containing pump noise. The noise is significantly reduced in 10b after the filter application – as indicate by the removal of the red-line, narrow band pump noise.

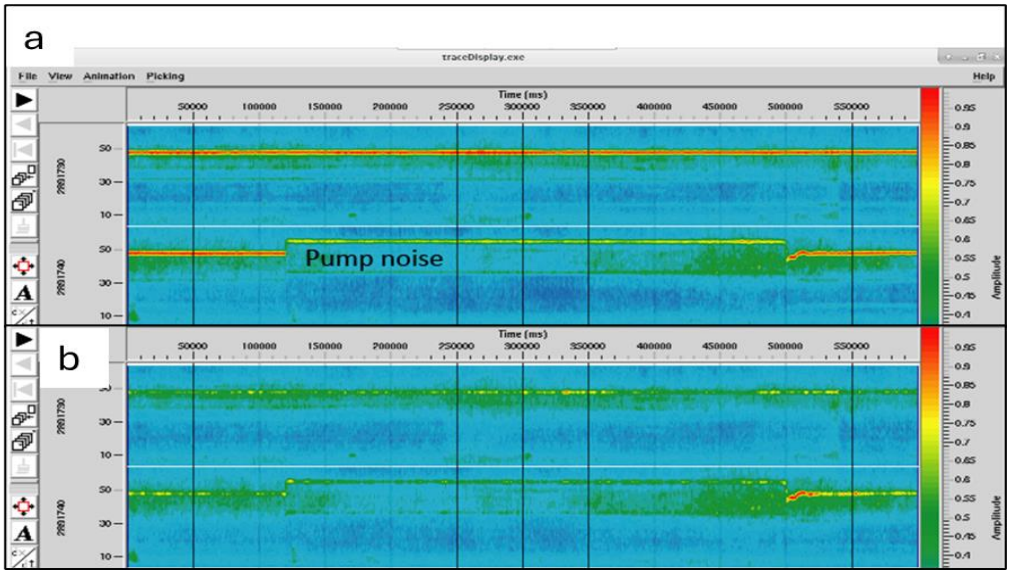

Figure 10. Cepstral Filtering to remove continuous steady noise. The spectrogram in (a) reveals the continuous narrow frequency band noise from a well pump on stations near Well 55-29 (the red lines at 49 Hz). The spectrogram in (b) is after Cepstral Filtering [2].

4.2 The Final Velocity Model.

Our pre-survey study of the available velocity models established a good baseline for seismic speeds below several hundred meters. However, due to significant topographic features in the study area, plus a comparative slow velocity near surface layer, estimation of 3D seismic travel times is required to perform the final PFI imaging step. A 3D velocity model was developed using a flat image datum at the elevation of 2000 m. To build the velocity model, small time shifts were added to re-datum the receiver data from the surface to a smoothed elevation-based surface shown in Figure 11a. The final step involved filling the shallow velocity layer to the 2,000 m-datum elevation (A. Stroujkova, personal communication 2020). Figure 11b shows the slice through the final 3D velocity model.

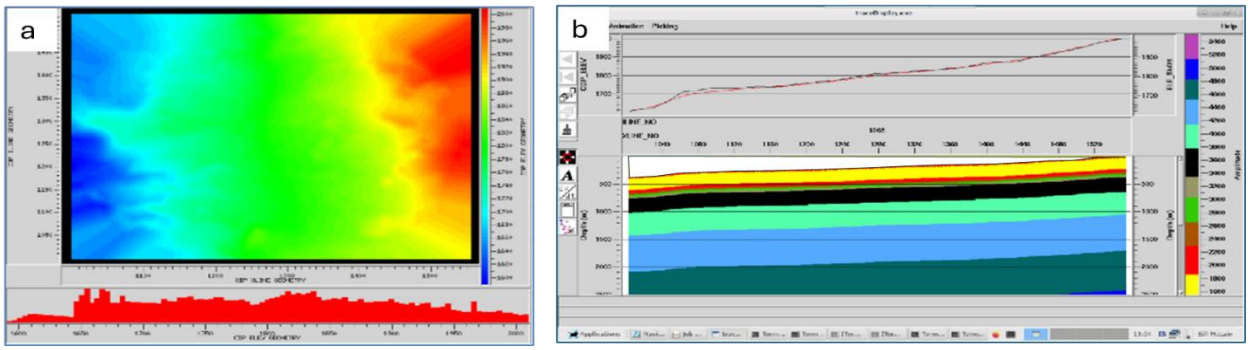

Figure 11. (a) Node elevations interpolated on 10 x 10 grid. (b) Linear E-W slice of the smoothed final 3D velocity model.

4.3 One-way Travel Time Depth Migration for PFI Signal Sources

The PFI signals observed by the seismic network can now be relocated to their origin points. The subsurface below the seismic network was first divided up into a rectangular prism containing 5,036,625 voxels, each measuring 10x10x10 m on side: 165 x 165 voxels in map view, and 185 in depth below a 250 m datum. (Above this depth the station spacing is too large for forming a PFI map.) The velocity model is used to compute the travel time from each voxel to each surface station. The observed data are then adjusted so that the signals appear at the same time for a selected voxel.

We then use a measure of the signal intensity and coherence for that voxel for a short time window (0.1 s) over the whole, noise suppressed, focused, aperture of receivers (the circle in Figure 7b). This measure is computed for every voxel in the depth volume for every time window in the quiet data set using semblance (S) defined as:

$$S = \frac{\sum_{j=0}^{T}\left[\sum_{i=0}^{K} f_{ij}(\tau_i)\right]}{\sum_{j=0}^{T}\sum_{i=0}^{K} f_{ij}^{2}(\tau_i)}, \qquad (1)$$

where K is the number of time samples in each window, T is the number of traces, and $f_{ij}(\tau_i)$ is the trace value at the time τ_i. Using semblances ensures that all values in the intensity volumes are positive. This value is migrated back to a subsurface voxel and recorded there. This is known as Kirchhoff depth migration. The same procedure is repeated for every voxel in this same time window, filling the prism with values. This is then repeated for seconds to minutes until an ensemble of volumes has been collected - the number of which is tested for what gives the best final image – which are then stacked together. These steps are illustrated in Figure 12.

It is notable that microearthquakes that appear in these time windows are used to check the focusing, which depends critically on having an accurate velocity model. When the model is accurate, the earthquake focuses into one voxel. After checking, these events are deliberately removed so as not to interfere with the much lower energy PFI signals.

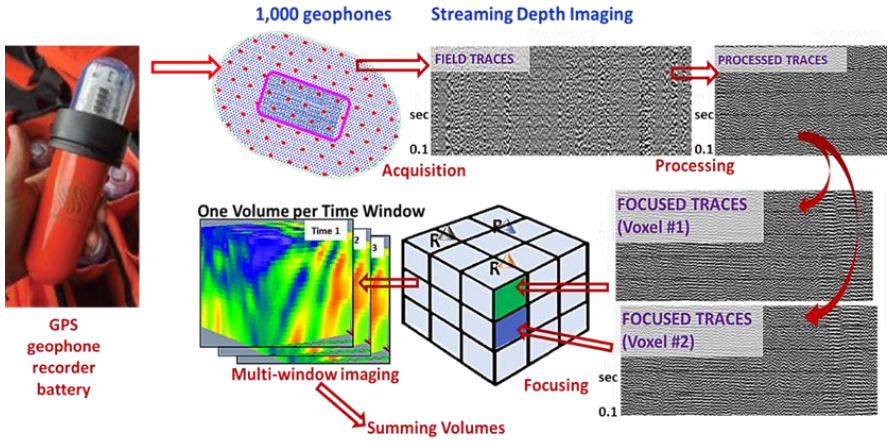

Figure 12. The PFI workflow from node to summed volume of signals for each voxel, yielding the final 3 D volume of relative signals. In this way a "stacking fold" of many hundreds of thousands of images is achieved.

5. FINAL PFI VOLUMES: A VISUAL DESCRITION.

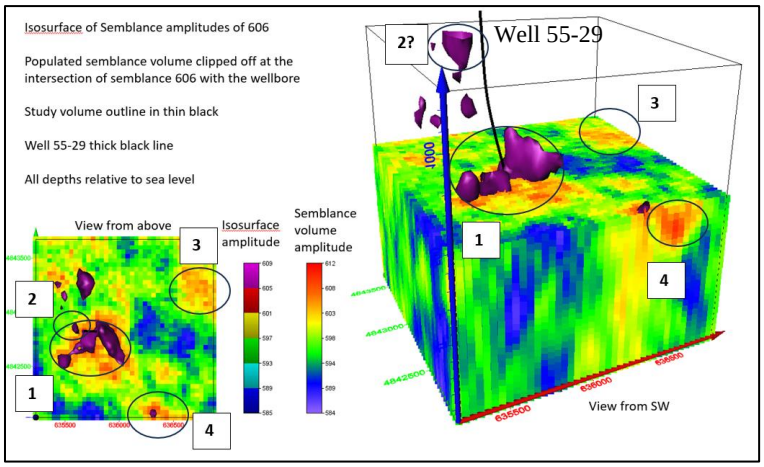

Figure 13 The final PFI volume, with the top 2/3 of volume showing only S values above a threshold. The lower 1/3 shows all values. The 1400 m deep map slice on the left (top of the block on the right) reveals: 1. A volume of high PFI signals near the 55-29 Well; 2. Smaller shallow volumes; 3. and 4. High threshold voxels embedded in the lower half block.

Figure 13 provides 2 views of the PFI volume, a map slice and a cut-away block, both at 1400 m below ground. There are 4 features of note in these views, a relatively large volume of near-well high PFI values; and 3 off well volumes. These same features are seen in progressive vertical slices approaching Well 55-29 from the north and south (Figure 14). Figure 15 shows map slices at 1280 m and 1360 m, revealing a strong NNW trend in PFI maps.

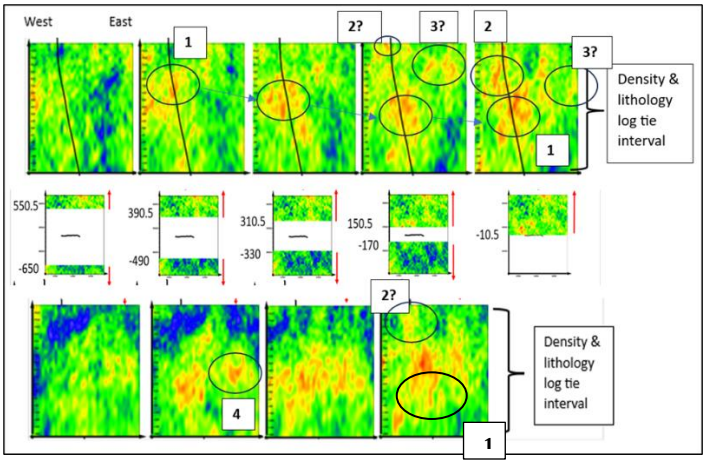

Figure 14. Top, vertical slices to the north of Well 55-29. Center, map view of the slice locations north and south of Well 55-29. Bottom, vertical slices to the south of Well 55-29. A high semblance PFI feature, correlated with Feature 1 in Figure 13, progresses southward to deeper depths and intersects with Well 55-29. A second Feature, indicated by 2, appears to follow Feature 1, but begins a few hundred meters above to the north. Features 3 and 4 appear respectively north and south of the well.

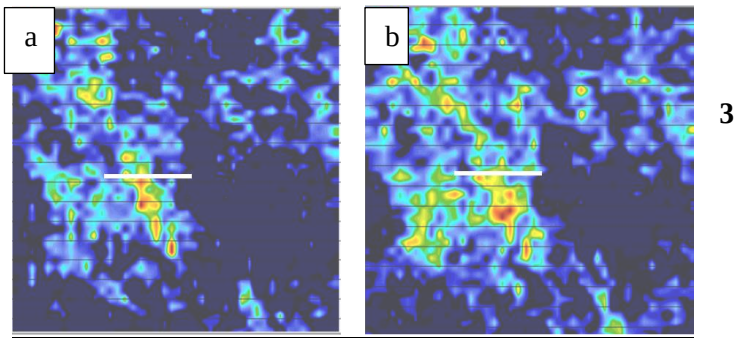

Figure 15 (a) 1280 m depth slice, and (b) 1360 m depth slices. Note the NNW and WSW tends in these PFI images.

6. FINAL PFI VOLUMES: A GEOLOGICAL INTERPRETATION IN FIGURES

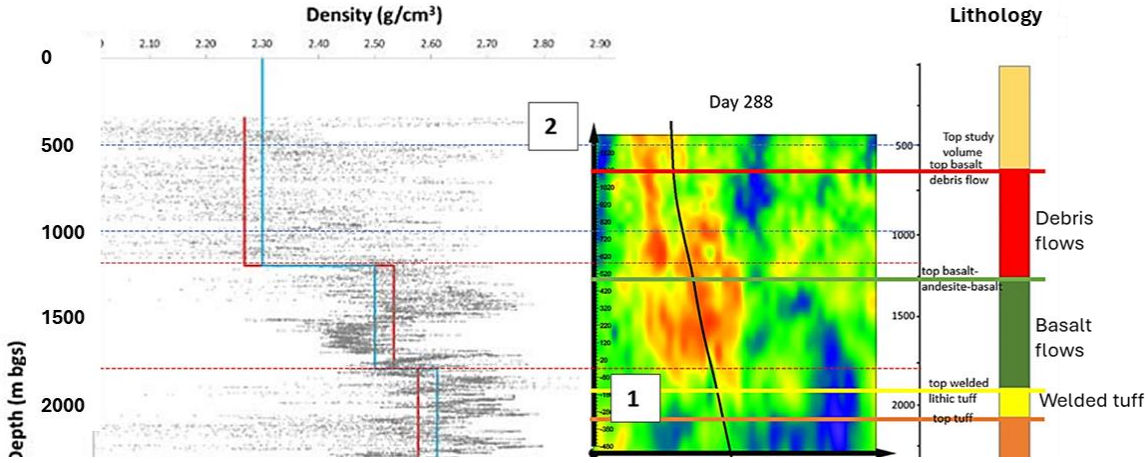

Figure 16. The density and lithology logs of the 55-29 Well placed against the vertical PFI section through the Well. The two PFI labeled zones, 1 and 2, correspond to those in Figures 13 and 14. Typical of seismic observations, the PFI section corelates best with density, as it is a determinant of seismic source and wave propagation properties. The PFI signals above both the density and debris flow are more related to fractures, a correlation that becomes clearer when compared with the resistivity.

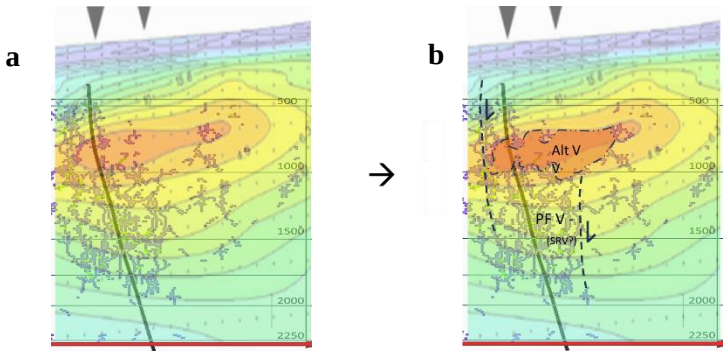

Figure 17. (a) Vertical cross section through the cloud of PFI activity shown in Figure 16, now displayed using the traces of cloud's local maxima. These are the *tracks* of connected voxels within the cloud, inter showing the central permeability channel. (b) The PFI map interpreted in terms of normal faults and the low permeability clay cap observed in the resistivity data.

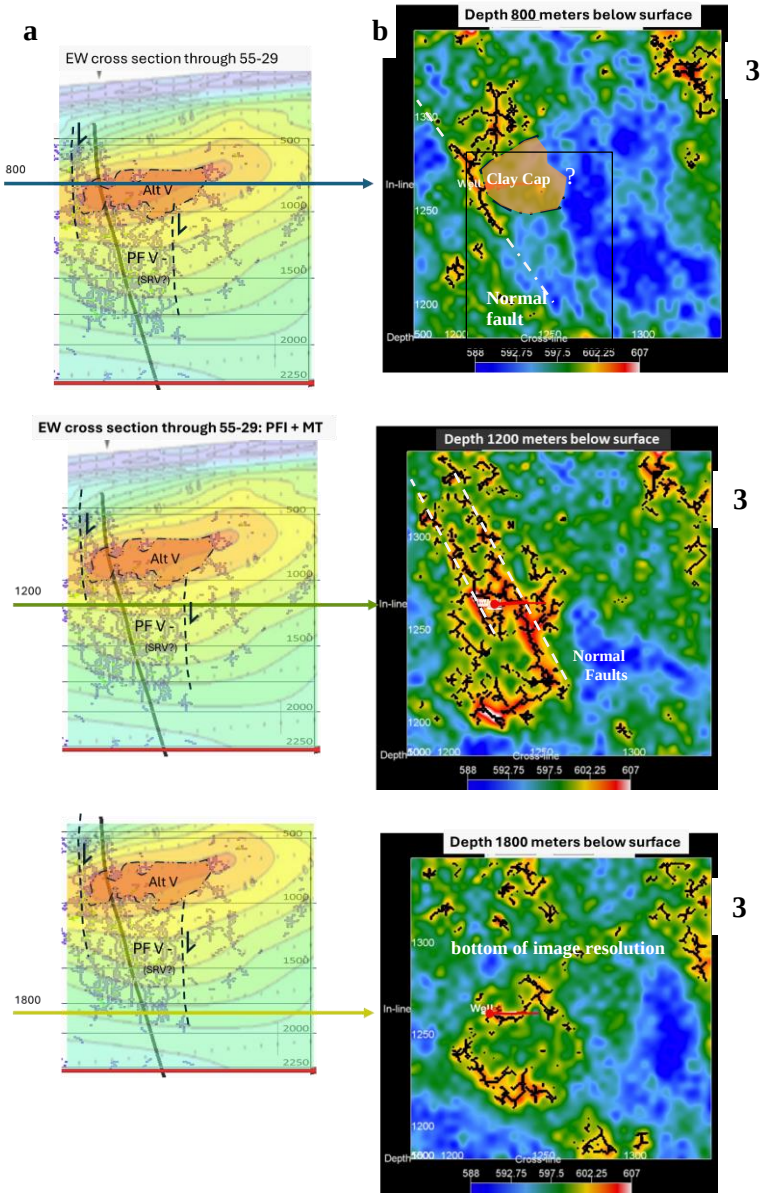

Figure 18. Column (a) PFI cross sections through Well 55-29. The arrows point to the corresponding depth slice in Column (b) at the indicated depth. Both the cross sections and maps have been interpreted as mapping the highly conductive, but low permeability clay cap (top row), normal faults with surrounding fluid-filled fractures (middle row), and the depth at which the Newberry PFI data collection network begins to lose PFI resolution. The 3 label corresponds to Figures 13, 14, and 15.

7. CONCLUSIONS

The field program faced the challenge of recording in a volcanic terrain and characterizing a proper velocity model. Despite these challenges, our Newberry passive seismic Permeable Fracture Imaging project has produced robust results. The project has provided a basic demonstration of the PFI technique in volcano-associated superhot geothermal applications. The results show that:

- The near-well PFI results appear to correlate best with the density log in Well 55-29.
- The PFI sections appear to cross lithology boundaries, reflecting their origins in fractures rather than rock type.
- The imagery shows an active fluid filled fracture system that extends beyond 55-29 for a couple of hundred meters.
- Sharp, NNW trending edges in the PFI data coincide with orientation of regional normal faults
- The low resistivity in the MT data is interpreted in the PFI data as a low permeability clay cap, plugging the fractures.
- Compared to the MT data, the PFI resolution is about one to two orders of magnitudes finer.

Our ARPA-E funded SEED grant, and our industry sponsor, have been instrumental in helping us demonstrating PFI technology in geothermal applications. Our original budget limitations constrained our ability to image deeper than ~2100 m. To achieve deeper PFI results, down to the ~3,000 m objective of Well 55-29, half-again more stations and a 38 square km area compared to the 27 square km we used in 2023 are needed. Fortunately, we have received the support necessary for this expansion, to take place in the summer of 2025.

REFERENCES

[1] Geiser, P. A., Malin, P. E., Boyer, S. E., Geiser J. R., Permeability field imaging: Mapping the geocritical crust's permeability field. *AAPG Bulletin* 2023;; 107 (9): 1581–1608. doi: https://doi.org/10.1306/05032322030

[2] Sicking, C.; Malin, P. Fracture Seismic: Mapping Subsurface Connectivity. *Geosciences* **2019**, *9*, 508. https://doi.org/10.3390/geosciences9120508

[3] Newberry Geothermal Energy, Establishment of the Frontier Observatory for Research in Geothermal Energy (FORGE) at Newberry Volcano, Oregon, Appendix A Conceptual Geologic Model, 2016.

[4] Cladouhos, T. T., Petty, S., Swyer, M. W., Uddenberg, M., and Nordin, Y., "2014 Results from Newberry Volcano EGS Demonstration," AltaRock Energy Inc., 2015.

[5] Cladouhos, T. T., Petty, S., Nordin, Y., Garrison, G., Uddenberg, M., Swyer, M. and Grasso, K., "Newberry Enhanced Geothermal Systems Demonstration Phase 2.1 Report," AltaRock Energy, Inc., 2014.

[6] Crider, J. G., Oblique slip and the geometry of normal-fault linkage: mechanics and case study from the Basin and Range in Oregon, *Journal of* Structural Geology, vol. 23, pp. 1997-2009, 2001.

[7] Robinson, J., Donnelly-Nolan E. J., and Jensen, R. A. Newberry Volcano's Youngest Lava Flows, U.S. Geological Survey, 2015

[8] MacLeod, N. S., Sherrod, D. R., Chitwood, L. A., and Jensen, R. A., Geologic Map of Newberry Volcano, Deschutes, Klamath, and Lake Counties, Oregon, U.S. Geological Survey, 1995.

[9] Waibel, A. F. Frone Z., and Jaffe, T., Geothermal exploration at Newberry Volcano, central Oregon, 2012.

[10] Beachly, M. W. Hooft, E. E. Toomey D. R. and Waite, G. P. Upper crustal structure of Newberry Volcano from P-wave tomography and finite difference waveform modeling, Jounral of Geophysical Research, vol. 117, no. B10, 201

[13] Foulger Consulting, Newberry Calibration Shot Project. Internal Report to AltaRock Energy, Inc., 2010.

[14] Pinzon-Rincon, L. Lavoué, F. Mordret A., Boué, P. Brenguier, F. Dales P., Ben-Zion Y., Vernon F., Bean C. J.and Hollis D., Humming Trains in Seismology: An Opportune Source for Probing the Shallow Crust, SRL, vol. 92, no. 2A, pp. 623-635, 2021.

[15] Cotton J. and Catchings, R. Data report from the 1983 US Geological Survey East-central Oregon Seismic Refraction Experiment, U.S. Geological Survey, 1989.

[16] Dawson P. B. and Stauber, D. A. Data report for a three-dimensional high-resolution P-velocity structural investigation of Newberry Volcano, Oregon, using seismic tomography, U.S. Geological Survey, 1986.

[17] Catchings R. and Mooney, W. Crustal structure of east central Oregon: Relation between Newberry Volcano and regional crustal structure, Journal of Geophysical Research, vol. 93, no. B9, pp. 10081-10094, 1988.

[18] Heath, B. A. Hooft, E. E. Toomey D. R. and Bezada M. J., Imaging the magmatic system of Newberry Volcano using joint active source and teleseismic tomography, Geochemistry, Geophysics, Geosystems, vol. 16, 2015.

[19] Templeton D. C., Matzel, E. Johannesson, G. Myers S. C. and Goebel M., Final Report: Mapping Fracture Network Creation with Microseismicity During EGS Demonstrations, Lawrence Livermore National Lab, 2014.